

SynTable: A Synthetic Data Generation Pipeline for Unseen Object Amodal Instance Segmentation of Cluttered Tabletop Scenes

Zhili Ng* Haozhe Wang*,[†] Zhengshen Zhang* Francis Eng Hock Tay
 Marcelo H. Ang Jr.

Advanced Robotics Centre, National University of Singapore

{ng.zhili, wang.haozhe, zhengshen_zhang}@u.nus.edu, {mpetayah, mpeangh}@nus.edu.sg

Abstract

In this work, we present *SynTable*, a unified and flexible Python-based dataset generator built using NVIDIA’s Isaac Sim Replicator Composer for generating high-quality synthetic datasets for unseen object amodal instance segmentation of cluttered tabletop scenes. Our dataset generation tool can render a complex 3D scene containing object meshes, materials, textures, lighting, and backgrounds. Metadata, such as modal and amodal instance segmentation masks, occlusion masks, depth maps, bounding boxes, and material properties can be generated to annotate the scene according to the users’ requirements automatically. Our tool eliminates the need for manual labeling in the dataset generation process while ensuring the quality and accuracy of the dataset. In this work, we discuss our design goals, framework architecture, and the performance of our tool. We demonstrate the use of a sample dataset generated using *SynTable* by ray tracing for training a state-of-the-art model, UOAI-Net. The results show significantly improved performance in Sim-to-Real transfer when evaluated on the OSD-Amodal dataset. We offer this tool as an open-source, easy-to-use, photorealistic dataset generator for advancing research in deep learning and synthetic data generation. The source code for our work is available at <https://github.com/ngzhili/SynTable>. The links to our demonstration video and our sample dataset can be found in the supplementary materials.

1. Introduction

Amodal completion is a perceptual ability that enables the perception of whole objects, even when they are partially occluded [1, 16]. Humans are capable of “filling in” the occluded appearance of invisible objects, owing to their vast experience in perceiving countless objects in various con-

*These authors contributed equally to this work.

[†]Corresponding author.

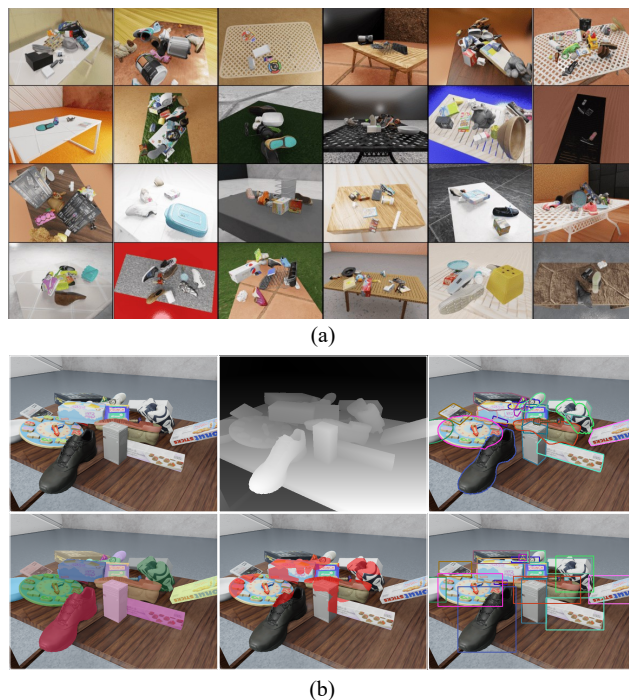


Figure 1. (a) Sample RGB outputs of photorealistic cluttered tabletop scenes generated by SynTable pipeline. (b) Visualization of RGB Images, Depth Images, Object Amodal Masks, Object Visible Masks, Object Occlusion Masks, and Object Visible Bounding Boxes. This figure is best viewed zoomed in.

texts and scenes. This ability to perceive an entire object based on its partial appearance is crucial in enabling reliable and accurate planning of subsequent actions. In modern autonomous robotic systems, comprehending objects in an environment is essential for numerous applications. In vision-based robotic grasping, deep learning perception algorithms are important in extracting critical information about objects in a scene, including their category, shape, appropriate grasping points, and occlusion information. In robotic grasping systems, the ability to infer an occluded object’s complete structure from its visible components al-

lows the robot to plan the grasp order and safely grasp novel occluded objects in cluttered scenes with greater precision and robustness.

There are three acute robotic perception challenges related to amodal instance segmentation: Firstly, the lack of large-scale, high-quality datasets for unseen object amodal instance segmentation (UOAIS) prevents some vision-based grasping systems from achieving their best performance [3]. There are several well-known grasp generation datasets [7, 11, 15, 17, 29]. Still, very few datasets focus on UOAIS [2]. This could be because such datasets are challenging to annotate manually and accurately. While it is possible to annotate grasp poses manually [5, 15, 30], human-annotated amodal instance segmentation masks [2] could be highly subjective and prone to errors. These human annotations are therefore considered imperfect ground truths.

Secondly, although it is possible to generate large synthetic datasets in a simulation environment [28], the issue of visual domain mismatch results in a poor Sim-to-Real transfer that will inevitably reduce the performance of algorithms in real-world applications. This could be because of a lack of domain randomization or because the software generates non-photorealistic scenes for synthetic data.

Thirdly, there is currently a lack of tools available to automatically generate amodal instance segmentation mask annotations to train the amodal completion capability of robotic grasping systems. There is also no effective metric to accurately evaluate a perception model’s ability to determine the occlusion order relationship of objects in a scene. The capacity for amodal completion and adequate comprehension of occlusion relationships between objects within a given scene are crucial for robots working in highly cluttered environments. Amodal completion can aid the planning of pick sequences and avoid collisions with other objects in grasping tasks. However, creating amodal annotations is a task that demands significantly more effort and skill from human annotators than creating modal annotations. Consequently, obtaining amodal annotations through manual annotation is an extremely time-consuming and costly process. For this reason, generating amodal annotations using simulation tools is a much more desirable option.

In this work, we aim to address these three challenges by building a unified and flexible Python-based tool to generate customizable, high-quality, and photorealistic datasets for UOAIS of cluttered tabletop scenes. We focus our work on cluttered tabletop scenes as tabletops are a common place where grasping and manipulation tasks are performed. We develop a novel unified framework that combines the rendering and annotation of scenes and objects in a dataset into a single pipeline. Users can customize the type of scene rendered, the number and variety of objects in the scene,

and the types of annotations required for their dataset. Our tool is built on NVIDIA’s Isaac Sim Replicator Composer to leverage its high-fidelity graphics rendering capability.

Our key contributions are summarized as follows:

1. We develop a pipeline to automatically render photorealistic cluttered tabletop scenes and generate ground truth amodal instance segmentation masks. This eliminates the need for any manual labeling in the dataset generation process while ensuring the quality and accuracy of the dataset. Based on our pipeline, we designed a dataset generation tool to create photorealistic and accurately-labeled custom datasets for UOAIS (refer to Figure 1(a)). Our tool can be easily added to NVIDIA Isaac Sim to leverage its ability to render complex and photorealistic 3D scenes with high fidelity.
2. Our tool provides a rich set of annotations related to amodal instance segmentation (refer to Figure 1(b)): modal (visible) and amodal instance segmentation masks, occlusion masks, occlusion rates, and occlusion order adjacency matrix. Users can easily select which annotations to include in their dataset based on the requirements of their application.
3. We proposed a novel method to evaluate how accurately an amodal instance segmentation model can determine object occlusion ordering in a scene by computing the scene’s Occlusion Order Accuracy (ACC_{OO}).
4. We generate a large-scale sample synthetic dataset using our tool consisting of amodal instance segmentation labels for users to train and evaluate their models on novel objects. Our dataset will be made publicly available.

2. Related Works

2.1. Amodal Instance Segmentation in Robotics

In recent years, there has been growing interest in developing amodal instance segmentation methods to enable more robust object detection and tracking in complex scenes. However, several limitations have been encountered in research on amodal instance segmentation in robotic grasping, such as the dearth of large-scale, high-quality training data and visual domain mismatch resulting in poor Sim-to-Real transfer.

Lack of Large-scale High-quality Training Data. Recently, a number of amodal datasets [8, 10, 31] have been developed for indoor scenes. However, there is a lack of high-quality datasets designed for amodal instance segmentation related to robotic grasping and manipulation tasks in cluttered tabletop scenes. Gilles *et al.* [13] recently presented a new benchmark dataset for evaluating the performance of ambidextrous grasping systems in bin-picking scenarios. Nevertheless, their work is limited in terms of scene diversity and object variety and may not be widely applicable beyond the bin-picking scenario. Richtsfeld *et*

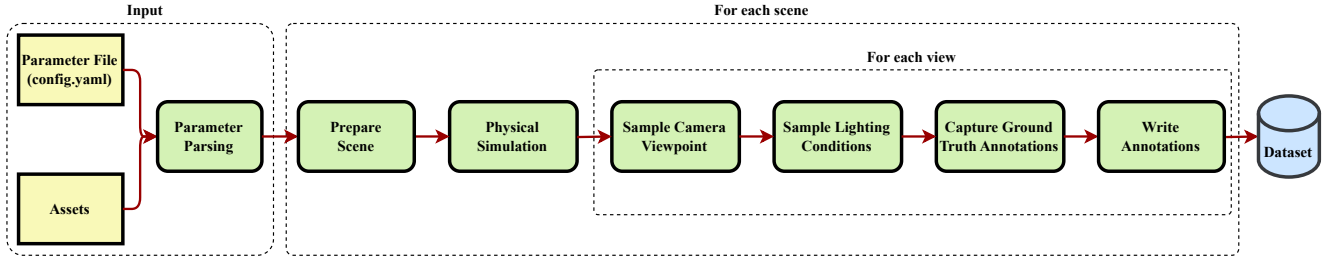


Figure 2. High-level overview of synthetic data generation pipeline.

al. [23] proposed the Object Segmentation Database (OSD) to facilitate the development of object segmentation algorithms in robotics and computer vision systems. Suchi *et al.* [24] designed a semi-automatic labeling tool to produce the Object Cluttered Indoor Dataset (OCID). Despite these efforts, neither OSD nor OCID includes amodal instance segmentation masks in their annotations. Recently, Back *et al.* [2] introduced amodal annotations to OSD. Nevertheless, this was done manually, which could be a time-consuming and error-prone process.

Sim-to-Real Problem. Xie *et al.* [28] created the Tabletop Object Dataset (TOD), a dataset comprising scenes that lack photorealism. This characteristic, coupled with the lack of domain randomization, might result in a significant Sim-to-Real gap. The UOAIS-Sim Dataset [2] also shares this limitation, as it lacks domain randomization as well.

2.2. Tools for Generating Synthetic Datasets

With the rapid development of deep learning, the demand of researchers for synthetic datasets has increased in recent years, which has led to the rise of the development of various tools for generating these datasets [27]. For robotics and computer vision applications, PyBullet and MuJoCo [26] are commonly used physical simulators for generating synthetic data. Xie *et al.* [28] pre-trained an RGB-D unseen object instance segmentation model using PyBullet. Tobin *et al.* [25] used MuJoCo to generate synthetic images with domain randomization, which can bridge the Sim-to-Real gap by realistically randomizing 3D content. Simulation tools such as PyBullet and MuJoCo typically come with renderers that are accessible and flexible, but they lack physically based light transport simulation, photorealism, material definitions, and camera effects.

To obtain better rendering capabilities, researchers also explored the use of video game-based simulation tools, such as Unreal Engine (UE4) or Unity 3D. For example, Qiu and Yuille [22] exported specific metadata by adding a plugin to UE4. Besides, Unity 3D can generate metadata and produce scenes for computer vision applications using the official computer vision package. Although game engines provide the most advanced rendering technology, they prioritize frame rate over image quality and offer limited capabil-

ities in light transport simulation.

Ray-tracing technology has gained significant traction in creating photorealistic synthetic datasets, as it enables the simulation of light behavior with high accuracy. Software applications such as Blender, NVIDIA OptiX, and NVIDIA Isaac Sim have all incorporated ray-tracing techniques into their functionality. The Replicator Composer, a component of NVIDIA Isaac Sim, constitutes an excellent tool for creating tailored synthetic datasets to meet various requirements in robotics. In this work, we leverage this platform to design a customized pipeline to generate a synthetic dataset tailored to the specific demands of UOAIS for cluttered tabletop scenes.

3. Method

Our dataset generation pipeline is illustrated using the diagram in Figure 2. We use a YAML file to store the parameters and configurations of the scenes to be rendered. The objects and settings required to render the scene are retrieved based on the instructions in the configuration file. We collectively term the objects, materials, and light sources used in our pipeline as assets. Thereafter, the tabletop scene with objects floating above the table is rendered in Isaac Sim. We then run a physical simulation to drop the rendered objects onto the table. For every view within a scene, camera viewpoints and lighting conditions are re-sampled. Subsequently, ground truth annotations are obtained and systematically recorded to create the dataset.

3.1. Preparing Each Scene

The method to prepare each scene is shown in Figure 3. A table is randomly sampled from the assets in Omniverse Nucleus and is rendered at the center of a room. The texture and materials of the table, ceiling, wall, and floor are randomized for every scene to ensure domain randomization. The objects are added to the scene with randomized x , y , and z coordinates and orientations. We randomly sample (with replacement) N_{lower} to N_{upper} objects to render for each scene. By default, $N_{lower} = 1$, $N_{upper} = 40$. Each object is initialized with real-life dimensions, randomized rotations and coordinates, allowing for diverse object arrangements across scenes. Each object also has mass and colli-

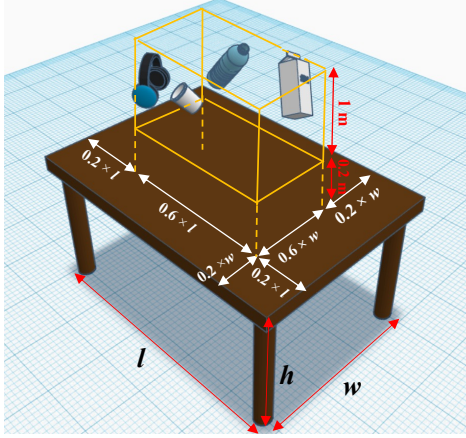


Figure 3. Initialization of objects with randomized coordinates and rotations. The initial position of the objects in the scene is randomized but constrained to be within the dimensions of the 3D orange box. The orange box is 0.2 m above the tabletop. The roll, pitch, and yaw of each object are also randomly sampled within the range of 0° to 360° .

sion properties so that they can be dropped onto the tabletop in our physics simulation.

3.2. Physical Simulation of Each Scene

Upon completing the scene preparation, the rendered objects are dropped onto the table surface using a physics simulation. The simulation is paused after t seconds ($t = 5$ by default), halting any further movement of the objects. During the simulation, any objects that rebound off the tabletop surface and fall outside the spatial coordinate region of the tabletop surface (i.e., either below the table or beyond the width and length of the table) are automatically removed. This is necessary to prevent the inclusion of extraneous and irrelevant objects outside the specified tabletop region during the annotation process from different viewpoints.

3.3. Sampling of Camera Viewpoints

To capture annotations for each scene from multiple viewpoints, we enhance the approach by Gilles *et al.* [18]—which only uses fixed viewpoint positions—by introducing a feature that captures V number of viewpoints at random positions within two concentric hemispheres, as illustrated in Figure 4. V can be set by the user. The radii of the two concentric hemispheres are uniformly sampled within the range r_{view_lower} m to r_{view_upper} m, where r_{view_lower} and r_{view_upper} are defined in Equations 1 and 2. Users may also set fixed values for r_{view_lower} and r_{view_upper} should they wish to do so.

$$r_{view_lower} = \max\left(\frac{w}{2}, \frac{l}{2}\right) \quad (1)$$

$$r_{view_upper} = 1.7 \times r_{view_lower} \quad (2)$$

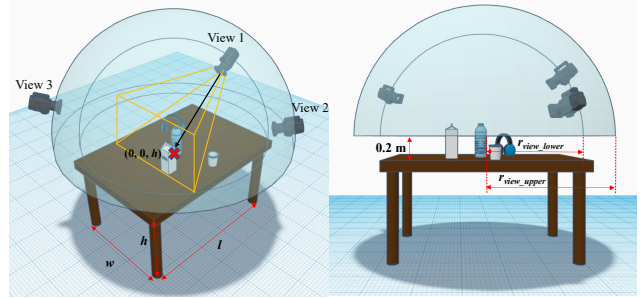


Figure 4. Sampling of camera viewpoints within concentric hemispheres (shown in blue). The two concentric hemispheres' origins are centered at the tabletop surface's center coordinate with an offset of 0.2 m in the positive z direction in the world frame. This allows the camera viewpoints to minimally have a direct line of sight to the tabletop surface to capture part of the tabletop plane. This figure is best viewed zoomed in.

The hemisphere's spherical coordinates are parameterized using three variables r_{view} , u , and v . To generate the camera coordinates in the world frame, we first obtain the radius of the hemisphere r_{view} by uniform sampling between r_{view_lower} and r_{view_upper} . Next, we uniformly sample $u, v \in [0, 1]$, then substitute all the sampled values into Equations 3, 4 and 5 to compute the cartesian coordinates of the camera.

$$x = r_{view} \sin(\arccos(1 - v)) \cos(2\pi u) \quad (3)$$

$$y = r_{view} \sin(\arccos(1 - v)) \sin(2\pi u) \quad (4)$$

$$z = r_{view} \cos(\arccos(1 - v)) \quad (5)$$

Once the camera coordinates are set, the orientation of each camera is set such that each viewpoint looks directly at the center of the tabletop surface $(0, 0, h)$.

3.4. Sampling of Lighting Conditions

To simulate different indoor lighting conditions, we resample L spherical light sources between L_{lower} to L_{upper} for each viewpoint (Figure 5). By default, we set L_{lower} and L_{upper} to be 0 and 2, respectively. To position L spherical light sources for a viewpoint, we adopt a similar approach to the camera viewpoint sampling method discussed in Section 3.3. In contrast to the approach by Back *et al.* [2], we use spherical light sources that emit light in all directions. Furthermore, we uniformly sample light source temperatures between 2,000 K to 6,500 K. The default light intensity of each light source is uniformly sampled between 100 lx to 20,000 lx, and the default light intensity of ceiling lights in the scene is also sampled uniformly between 100 lx to 2,000 lx. To achieve diverse indoor lighting conditions for tabletop scenes, users have the flexibility to adjust the number of spherical light sources, as well as their intensities and temperatures.

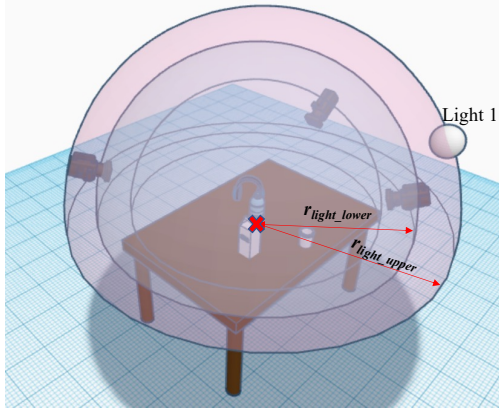


Figure 5. Sampling of lighting within concentric hemispheres (shown in pink). Each spherical light source lies within the constraints of two concentric hemispheres of arbitrary radius between r_{light_lower} to r_{light_upper} . Note that the radii constraints for the spherical light source concentric hemispheres are larger than those for the camera viewpoints’ and are customizable by the user.

Similar to the sampling method for the camera viewpoint coordinates, we have designed a feature that samples the lower and upper radii bounds for the light sources based on the camera hemisphere’s upper bound radius, r_{view_upper} . The sampled lower and upper bound radii constraints for the lighting hemisphere r_{light_lower} and r_{light_upper} are as follows:

$$r_{light_lower} = r_{view_upper} + 0.1m \quad (6)$$

$$r_{light_upper} = r_{light_lower} + 1m \quad (7)$$

3.5. Capturing of Ground Truth Annotations

The process of capturing the ground truth annotations for a scene is illustrated in Figure 6. At each view, the RGB and depth images of the tabletop scene will be captured (Figure 6(a)). The built-in instance segmentation function in Isaac Sim Replicator Composer is employed to capture the instance segmentation mask of the entire scene from a viewpoint (Figure 6(b)). Subsequently, each object’s visible mask is cropped from the instance segmentation mask of the scene. To obtain the amodal mask of each object on the simulated tabletop scene, we have developed the subsequent steps.

Initially, all objects’ visibility is disabled. For each object o within the scene, its visibility is enabled, and the instance segmentation function is utilized to capture its amodal mask (Figure 6(c)). Following this, we compute the object’s occlusion mask and occlusion rate, as presented in (Figure 6(d)). The occlusion mask of an object o can be acquired by subtracting its visible mask from its amodal mask.

The occlusion rate of the object o can be computed by dividing the number of pixels in the occlusion mask by the number of pixels in the amodal mask. If the occlusion rate of the object o is equal to 1, it implies that object o is completely obscured from the viewpoint, thus we do not save

the object o ’s annotation for this view. The visibility of object o is then disabled to capture the masks of the next object. Following the preservation of all objects’ masks, we use Algorithm 1 to generate the Occlusion Order Adjacency Matrix (OOAM) for this viewpoint (Figure 6(e)). For a scene with M objects, the OOAM contains $M \times M$ elements, where the element (i, j) is a binary value in the matrix which indicates whether object i occludes object j . Given the OOAM, we can easily construct the Occlusion Order Directed Graph (OODG) to visualize the occlusion order in the viewpoint (Figure 6(e)). We provide a detailed explanation of the OODG in our supplementary materials. After that, the visibility of all objects is enabled to prepare for the capturing of annotations from the next viewpoint of the scene.

Algorithm 1 A function to generate the OOAM of objects in a viewpoint.

Input: Arrays of *visibleMasks* and *occlusionMasks* of objects in a scene

Output: The OOAM of objects in a viewpoint

```

1: function GENERATE_OOAM(visibleMasks, occlusionMasks)
2:   Initialize OOAM as matrix of zeros
3:   for each object i in length(VisibleMasks) do
4:     for each object j in length(OcclusionMasks) do
5:       if (i != j): then
6:         intersect = sum(visibleMasks[i] ∩ occlusionMasks[j])
7:         if (intersect > 0): then
8:           OOAM[i][j] = 1
9:   return OOAM

```

10: **Note:** object *i* occludes object *j* if OOAM[*i*][*j*] = 1

4. Dataset Details

To demonstrate the capabilities of SynTable, we generated a sample synthetic dataset, SynTable-Sim, using our pipeline, for training and evaluating UOAIS models. Note that users can also generate other custom datasets that meet the specific requirements of their application using SynTable.

4.1. Object Models Used in Generating SynTable-Sim

We use 1075 object CAD models from the Google Scanned Objects dataset [9] and the Benchmark for 6D Object Pose Estimation (BOP) [14] for generating our train dataset. The Google Scanned Objects dataset features over 1030 photorealistic 3D scanned household objects with real-life dimensions, and BOP features 3D object models from household and industrial objects. As the context of our work is in robotic grasping, we only select objects that a parallel gripper can grasp to be part of our dataset. Upon inspection of the Google Scanned Objects dataset, we filter out invalid objects that contain more than two instances in each model and keep the remaining 891 valid objects for our training dataset. From the BOP, we exclude 21 objects from the YCB-Video dataset that we include in our validation dataset and use the remaining 184 objects for our training dataset.

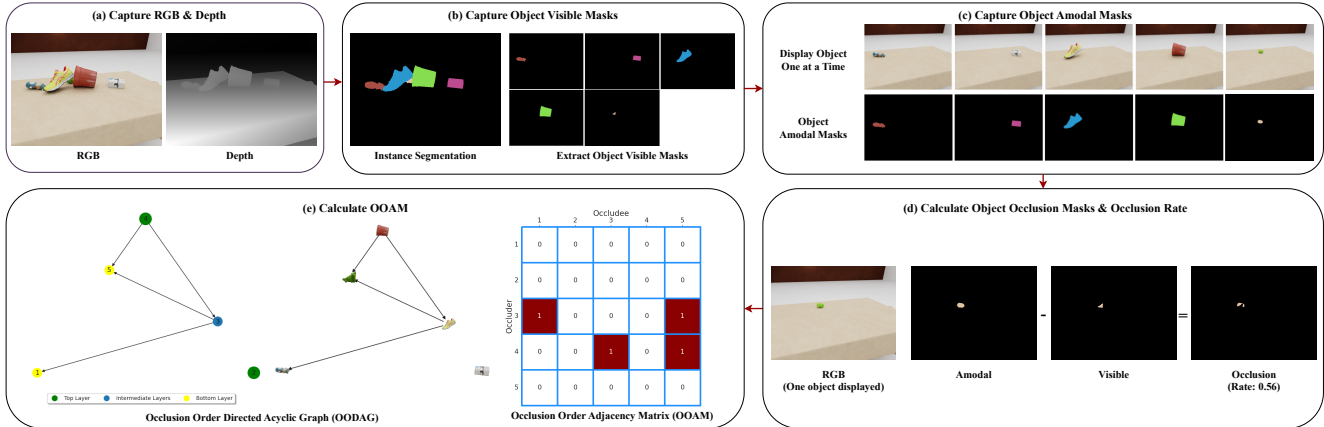


Figure 6. The process of capturing the ground truth annotations for a scene. For each viewpoint, we capture the following: (a) RGB and depth with all objects displayed, (b) object visible masks & bounding box, (c) object amodal masks, (d) object occlusion masks and occlusion rate, (e) occlusion order adjacency matrix. This figure is best viewed zoomed in.

Table 1. A comparison of publicly available unseen object instance segmentation datasets for cluttered tabletop scenes. # indicates the number of items. **VI**: Visible Instances. **OI**: Occluded Instances. **Avg. OR %**: Avg. Occlusion Rate %, i.e., the fraction of occluded pixels to amodal pixels across all object instances in the dataset. **AM**: Availability of amodal masks. **OM**: Availability of occlusion masks.

Order: Availability of occlusion order relation information between objects. **R/S**: Real or Synthetic. - indicates that the data was not available in the literature. * indicates that the values were not provided in the original literature, but we were able to compute the values.

Dataset	#Images	#Objects	#Scenes	#VI	#OI	Avg. OR (%)	AM	OM	Order	R/S
OCID [24]	2,390	89	96	19,097*	-	-	✗	✗	✗	R
OSD [23]	111	-	111	474*	-	-	✗	✗	✗	R
OSD-Amodal [2]	111	-	111	474*	237*	24.11*	✓	✓	✗	R
UOAIS-Sim (Tabletop) [2]	25,000	375	500	356,885*	127,129*	11.16*	✓	✓	✗	S
SynTable-Sim (Ours)	50,000	1075	1000	744,454	482,921	<u>17.56</u>	✓	✓	✓	S

We also create a synthetic validation set using 78 novel objects from the YCB dataset [4]. We sample a table object from 10 Omniverse Nucleus table assets to provide randomization for each scene. To load the 3D object models into Isaac Sim, we convert the OBJ and texture files to the Universal Scene Description (USD) format.

4.2. Dataset Configuration

With 50 viewpoints for each scene, we generated 900 scenes to create 45,000 RGB-D images for the training dataset and 100 scenes to create 5,000 RGB-D images for the validation dataset. $N_{lower} = 1$ to $N_{upper} = 40$ objects are rendered on randomly textured tabletop planes in each scene. We used 130 materials from the Omniverse Nucleus material assets to be applied randomly on the walls, floor, and table for domain randomization purposes. $L_{lower} = 0$ to $L_{upper} = 2$ spherical lights are sampled for each scene. The viewpoint and lighting hemisphere parameters are automatically sampled based on the table dimensions. The camera parameters used are horizontal aperture: 2.63, vertical aperture: 1.96, and focal length: 1.88 to mimic the configuration of the Re-

alSense LiDAR Camera L515. The rest of the parameters follow the default configurations of the pipeline.

4.3. Syntable-Sim Versus Other Cluttered Tabletop Datasets

We compare our SynTable-Sim dataset with several other cluttered tabletop datasets from previous works in Table 1. Our tabletop dataset is the only one providing all annotations related to amodal instance segmentation. Our dataset also has the most extensive variety of objects, the highest number of occlusion instances, and the second highest average occlusion rate. These characteristics make our dataset very challenging for amodal instance segmentation tasks.

5. Experiments

In this section, we present the results of our experiments aimed at evaluating the effectiveness of our dataset generation pipeline in producing synthetic datasets with good Sim-to-Real transfer performance. We use our SynTable-Sim sample dataset to train a state-of-the-art (SOTA) UOAIS

model, UOAIS-Net [2]. UOAIS-Net is then evaluated on the SynTable-Sim validation set and OSD-Amodal [2] test set. To verify to consistency of our results and also to further demonstrate the capability of SynTable to improve the performance of a variety of different UOAIS models, we also train and evaluate three other UOAIS models—Amodal MRCNN [12], ORCNN [12], ASN [21]—on the SynTable-Sim and OSD-Amodal datasets respectively. The results and analyses for these models are included in Section 12 of our supplementary materials.

5.1. Training Strategy

We train UOAIS-Net on the UOAIS-Sim tabletop and SynTable-Sim datasets using an NVIDIA Tesla V100 GPU with 16 GB of memory. For both datasets, we use 90% of the images for training and 10% for validation. To train UOAIS-Net using the UOAIS-Sim tabletop dataset, we use the same hyperparameters as Back *et al.* [2]. To train UOAIS-Net with SynTable-Sim, we modified the depth range hyperparameter, which is used to preprocess input depth images. Specifically, we changed the range from the 2500 mm to 40000 mm range set by Back *et al.* to a narrower range of 250 mm to 2500 mm. This adjustment is required because our dataset reflects real-world proportions and has a smaller depth range than the UOAIS-Sim dataset. We also use a similar training strategy for training Amodal MRCNN, ORCNN, and ASN.

5.2. Evaluation Metrics

We measure the performance of UOAIS-Net on the following traditional metrics [6, 19, 28]: Overlap P/R/F, Boundary P/R/F, and $F@.75$ for the amodal, visible, and invisible masks. Overlap P/R/F and Boundary P/R/F evaluate the whole area and the sharpness of the prediction, respectively, where P, R, and F are the precision, recall, and F-measure of instance masks after the Hungarian matching, respectively. $F@.75$ is the percentage of segmented objects with an Overlap F-measure greater than 0.75. We also report the accuracy (ACC_{θ}) and F-measure (F_{θ}) of occlusion classification, where $ACC_{\theta} = \frac{\delta}{\alpha}$, $F_{\theta} = \frac{2P_{\theta}R_{\theta}}{P_{\theta}+R_{\theta}}$, $P_{\theta} = \frac{\delta}{\beta}$, $R_{\theta} = \frac{\delta}{\gamma}$. α is the number of the matched instances after the Hungarian matching. β , γ , and δ are the number of occlusion predictions, ground truths, and correct predictions, respectively. We provide more details about the evaluation metrics in Section 8 of our supplementary materials.

Due to the subjectivity of the objects’ invisible masks, evaluating UOAIS model performance solely based on the overlap and boundary P/R/F of segmented objects may be inaccurate. The current UOAIS occlusion evaluation metrics measure how well the model can predict if individual objects are occluded. However, these metrics do not measure object occlusion ordering in a scene which would be helpful in scene understanding for robotic grasp planning.

The OOAM can represent a scene’s occlusion order, while the OODG can be derived from the OOAM. By knowing the occlusion order in a scene, a robot can use topological sorting of the predicted OODG to plan the order of grasping to reach the occluded object of interest. Thus, to evaluate the accuracy of object occlusion order in an image, we introduce a new metric called Occlusion Order Accuracy (ACC_{OO}) as stated in Equation 8.

$$ACC_{OO} = \frac{sum(similarityMatrix) - gtOOAMDiagonalSize}{gtOOAMSize - gtOOAMDiagonalSize} \quad (8)$$

In Equation 8, *similarityMatrix* is the element-wise equality comparison between the ground truth OOAM, *gtOOAM*, and the predicted OOAM, *predOOAM*. As an object cannot occlude itself, the diagonal of any OOAM is always 0. Thus, we subtract the number of elements along the diagonal of *gtOOAM*, *gtOOAMDiagonalSize*, from the calculation of ACC_{OO} . ACC_{OO} is used to evaluate the model’s ability to accurately determine the order of occlusions in a clutter of objects by comparing the OOAM generated by the model to the ground truth OOAM using Algorithm 2. We give a specific example of how to compute ACC_{OO} in Sections 9 and 10 of our supplementary materials.

Algorithm 2 Evaluating Occlusion Ordering Accuracy

- Input:** The arrays of the ground truth and predicted visible and occlusion masks (*gtVisible*, *gtOcclusion*, *predVisible*, *predOcclusion*)
- Output:** Scene occlusion order accuracy ACC_{oo}
- 1: *gtOOAM* = GENERATE_OOAM(*gtVisible*, *gtOcclusion*)
 - 2: Get groundtruth-prediction assignment pairs after Hungarian matching
 - 3: Extract *predVisible* and *predOcclusion* masks from assignment pairs
 - 4: *predOOAM* = GENERATE_OOAM(*predVisible*, *predOcclusion*)
 - 5: *similarityMatrix* = (*predOOAM* == *gtOOAM*) ▷ Compare the similarity between the predicted and ground truth OOAMs
 - 6: Calculate ACC_{oo} using Equation 8
-

5.3. Results

Table 2 compares the performance of UOAIS-Net on the OSD-Amodal dataset after training on the UOAIS-Sim tabletop dataset and our SynTable-Sim sample dataset. We conduct four sets of experiments. In each set of experiments, we vary the amount of data augmentation used and the size of the dataset we use for training. In our first set of experiments, we can see that the UOAIS-Net trained on the SynTable-Sim dataset significantly outperforms the UOAIS-Net trained on the UOAIS-Sim tabletop dataset in all metrics. Even when we train UOAIS-Net using a dataset of the same size as UOAIS-Sim (SynTable-Sim-0.5X), the performance is still remarkably better than the UOAIS-Net trained on the UOAIS-Sim tabletop dataset across all metrics. A detailed breakdown of the precision P, recall R, and F-measure F, and $F@.75$ scores for the amodal, invisible, and visible masks for our first set of experiments are shown

Table 2. The performance of UOAIIS-Net on the **OSD-Amodal dataset** after training on the UOAIIS-Sim and SynTable-Sim datasets. UOAIIS-Net is trained with RGB-D images. **CR**: Crop Ratio lower bound. **HF**: Horizontal Flip. **CA**: Colour Augmentation. **PD**: Perlin Distortion. **OV**: Overlap F-measure, **BO**: Boundary F-measure, **F@.75**: Percentage of segmented objects with an Overlap F-measure greater than 0.75, **F $_{\phi}$** : Occlusion F-Measure, **ACC $_{OO}$** : Occlusion Order Accuracy

No.	Training Set	Augmentation				Amodal Mask			Invisible Mask			Occlusion		Visible Mask			ACC $_{OO}$
		CR	HF	CA	PD	OV	BO	F@.75	OV	BO	F@.75	F $_{\phi}$	ACC $_{\phi}$	OV	BO	F@.75	
1	UOAIIS-Sim (Tabletop)	✗	✗	✗	✗	42.4	34.1	47.1	21.6	15.2	18.5	43.1	61.8	42.5	32.3	37.1	12.7
1	SynTable-Sim (Ours)	✗	✗	✗	✗	80.9	61.8	78.1	52.4	31.2	41.3	75.7	86.7	81.1	64.3	74.4	82.9
1	SynTable-Sim-0.5X (Ours)	✗	✗	✗	✗	80.7	63.8	77.3	51.9	30.2	42.9	75.7	84.1	80.5	65.4	71.7	82.7
2	UOAIIS-Sim (Tabletop)	0.8	✓	✗	✗	26.1	33.1	66.7	15.5	7.7	20.4	60.8	78.1	25.9	27.6	51.8	42.7
2	SynTable-Sim (Ours)	0.8	✓	✗	✗	67.7	56.0	81.2	49.4	30.1	48.6	72.5	89.8	71.8	61.3	78.2	86.6
2	SynTable-Sim-0.5X (Ours)	0.8	✓	✗	✗	75.6	61.2	83.5	53.6	31.2	48.5	75.5	90.1	76.8	64.5	78.3	87.0
3	UOAIIS-Sim (Tabletop)	0.8	✓	✓	✓	71.8	62.8	81.4	55.6	31.3	44.6	75.1	86.2	70.2	63.2	73.2	79.6
3	SynTable-Sim (Ours)	0.8	✓	✓	✓	78.3	58.8	81.9	54.0	29.7	43.9	66.6	93.2	79.2	60.4	77.2	87.7
3	SynTable-Sim-0.5X (Ours)	0.8	✓	✓	✓	74.0	57.5	83.3	49.2	23.9	41.0	65.7	93.4	74.2	59.2	79.2	87.6
4	UOAIIS-Sim (Tabletop)	0.5	✓	✓	✓	49.0	50.3	82.7	42.3	23.9	40.3	68.9	84.0	47.3	50.0	70.6	80.4
4	SynTable-Sim (Ours)	0.5	✓	✓	✓	64.4	51.5	84.3	47.3	24.2	47.4	60.0	91.9	65.3	53.7	78.2	87.0
4	SynTable-Sim-0.5X (Ours)	0.5	✓	✓	✓	55.0	47.2	85.9	43.2	22.0	48.4	55.4	91.5	55.3	46.6	76.9	87.8

Table 3. A breakdown of the evaluation results of UOAIIS-Net on the **OSD-Amodal dataset** for the first set of experiments after training on the UOAIIS-Sim and SynTable-Sim dataset. **P**: Precision, **R**: Recall, **F**: F-measure, **F@.75**: Percentage of segmented objects with an Overlap F-measure greater than 0.75, **F $_{\phi}$** : Occlusion F-Measure, **ACC $_{OO}$** : Occlusion Order Accuracy

Training Set	Amodal Mask							Invisible Mask							Visible Mask					Occlusion		ACC $_{OO}$		
	Overlap			Boundary			F@.75	Overlap			Boundary			F@.75	Overlap			Boundary			F@.75		F $_{\phi}$	ACC $_{\phi}$
	P	R	F	P	R	F		P	R	F	P	R	F	F@.75	P	R	F	P	R	F	F@.75	F $_{\phi}$	ACC $_{\phi}$	
UOAIIS-Sim (Tabletop)	35.9	65.4	42.4	31.4	42.8	34.1	47.1	55.9	24.5	21.6	45.3	19.3	15.2	18.5	36.2	61.3	42.5	30.8	39.2	32.3	37.1	43.1	61.8	12.7
SynTable-Sim (Ours)	81.0	82.5	80.9	59.1	66.8	61.8	78.1	69.3	51.8	52.4	34.6	42.6	31.2	41.3	80.1	83.2	81.1	62.4	68.1	64.3	74.4	75.7	86.7	82.9

Table 4. The performance of UOAIIS-Net on the **SynTable-Sim validation** dataset after training on the UOAIIS-Sim and SynTable-Sim datasets. UOAIIS-Net is trained with RGB-D images. **OV**: Overlap F-measure, **BO**: Boundary F-measure, **F@.75**: Percentage of segmented objects with an Overlap F-measure greater than 0.75, **F $_{\phi}$** : Occlusion F-Measure, **ACC $_{OO}$** : Occlusion Order Accuracy

Training Set	Amodal Mask			Invisible Mask			Occlusion		Visible Mask			ACC $_{OO}$
	OV	BO	F@.75	OV	BO	F@.75	F $_{\phi}$	ACC $_{\phi}$	OV	BO	F@.75	
UOAIIS-Sim (Tabletop)	38.0	37.8	35.9	14.1	12.9	7.6	47.2	72.9	40.4	38.9	34.8	31.6
SynTable-Sim (Ours)	84.5	78.4	75.6	41.4	37.7	21.5	76.1	82.4	86.8	81.8	74.4	77.5

in Table 3. We observe that except for the Boundary precision scores of the invisible masks, UOAIIS-Net achieves substantial improvements in all other metrics.

In the next three sets of experiments, we observe that even when we include data augmentation, the performance of UOAIIS-Net trained on the UOAIIS-Sim tabletop dataset is still worse than that trained on the SynTable-Sim dataset without using any data augmentation. We also provide images of the inference results on the OSD-Amodal dataset in Section 11 of our supplementary materials.

Similarly, from Table 4, the UOAIIS-Net model trained on the SynTable-Sim dataset also outperforms the one trained on UOAIIS-Sim tabletop dataset in all metrics when both models are benchmarked on SynTable-Sim validation dataset.

Our experiments demonstrate the effectiveness of our proposed dataset generation pipeline, SynTable, in improv-

ing the Sim-to-Real transfer performance of SOTA deep learning computer vision models for UOAIIS. These results also highlight the potential of SynTable for addressing the challenge of annotating amodal instance segmentation masks.

6. Conclusion

In conclusion, we present SynTable, a novel synthetic data generation pipeline for generating photorealistic datasets that facilitated amodal instance segmentation of cluttered tabletop scenes. SynTable enables the creation of complex 3D scenes with automatic annotation of diverse metadata, eliminating the need for manual labeling while ensuring dataset quality and accuracy. We demonstrate the effectiveness of the SynTable pipeline by generating a photorealistic amodal instance segmentation dataset and using it to train

UOAI-Net. As a result, UOAI-Net achieves significantly improved Sim-to-Real transfer performance on the OSD-Amodal dataset, particularly in determining the object occlusion order of objects in a cluttered tabletop scene.

References

- [1] Jiayang Ao, Krista A Ehinger, and Qihong Ke. Image amodal completion: A survey. *arXiv preprint arXiv:2207.02062*, 2022. 1
- [2] Seunghyeok Back, Joosoon Lee, Taewon Kim, Sangjun Noh, Raeyoung Kang, Seongho Bak, and Kyoobin Lee. Unseen object amodal instance segmentation via hierarchical occlusion modeling. In *2022 International Conference on Robotics and Automation (ICRA)*, pages 5085–5092. IEEE, 2022. 2, 3, 4, 6, 7
- [3] Shehan Caldera, Alexander Rassau, and Douglas Chai. Review of deep learning methods in robotic grasp detection. *Multimodal Technologies and Interaction*, 2(3), 2018. 2
- [4] Berk Calli, Arjun Singh, Aaron Walsman, Siddhartha Srinivasa, Pieter Abbeel, and Aaron M. Dollar. The ycb object and model set: Towards common benchmarks for manipulation research. In *2015 International Conference on Advanced Robotics (ICAR)*, pages 510–517, 2015. 6
- [5] Fu-Jen Chu, Ruinian Xu, and Patricio A. Vela. Real-world multiobject, multigrasp detection. *IEEE Robotics and Automation Letters*, 3(4):3355–3362, 2018. 2
- [6] Achal Dave, Pavel Tokmakov, and Deva Ramanan. Towards segmenting anything that moves. In *2019 IEEE/CVF International Conference on Computer Vision Workshop (ICCVW)*, pages 1493–1502, 2019. 7, 1, 2
- [7] Amaury Depierre, Emmanuel Dellandréa, and Liming Chen. Jacquard: A large scale dataset for robotic grasp detection. In *2018 IEEE/RSJ International Conference on Intelligent Robots and Systems (IROS)*, pages 3511–3516, 2018. 2
- [8] Helisa Dhano, Nassir Navab, and Federico Tombari. Object-driven multi-layer scene decomposition from a single image. In *Proceedings of the IEEE/CVF International Conference on Computer Vision (ICCV)*, 2019. 2
- [9] Laura Downs, Anthony Francis, Nate Koenig, Brandon Kinman, Ryan Hickman, Krista Reymann, Thomas B McHugh, and Vincent Vanhoucke. Google scanned objects: A high-quality dataset of 3d scanned household items. *arXiv preprint arXiv:2204.11918*, 2022. 5
- [10] Kiana Ehsani, Roozbeh Mottaghi, and Ali Farhadi. Segan: Segmenting and generating the invisible. In *Proceedings of the IEEE Conference on Computer Vision and Pattern Recognition (CVPR)*, 2018. 2
- [11] Hao-Shu Fang, Chenxi Wang, Minghao Gou, and Cewu Lu. Graspnet-1billion: A large-scale benchmark for general object grasping. In *2020 IEEE/CVF Conference on Computer Vision and Pattern Recognition (CVPR)*, pages 11441–11450, 2020. 2
- [12] Patrick Follmann, Rebecca König, Philipp Härtinger, Michael Klostermann, and Tobias Böttger. Learning to see the invisible: End-to-end trainable amodal instance segmentation. In *2019 IEEE Winter Conference on Applications of Computer Vision (WACV)*, pages 1328–1336, 2019. 7
- [13] Maximilian Gilles, Yuhao Chen, Tim Robin Winter, E. Zhixuan Zeng, and Alexander Wong. Metagraspnet: A large-scale benchmark dataset for scene-aware ambidextrous bin picking via physics-based metaverse synthesis. In *2022 IEEE 18th International Conference on Automation Science and Engineering (CASE)*, pages 220–227, 2022. 2
- [14] Tomáš Hodaň, Frank Michel, Eric Brachmann, Wadim Kehl, Anders Glent Buch, Dirk Kraft, Bertram Drost, Joel Vidal, Stephan Ihrke, Xenophon Zabulis, Caner Sahin, Fabian Manhardt, Federico Tombari, Tae-Kyun Kim, Jiří Matas, and Carsten Rother. BOP: Benchmark for 6D object pose estimation. *European Conference on Computer Vision (ECCV)*, 2018. 5
- [15] Yun Jiang, Stephen Moseson, and Ashutosh Saxena. Efficient grasping from rgb-d images: Learning using a new rectangle representation. In *2011 IEEE International Conference on Robotics and Automation*, pages 3304–3311, 2011. 2
- [16] Ke Li and Jitendra Malik. Amodal instance segmentation. In *Computer Vision – ECCV 2016*, pages 677–693, Cham, 2016. Springer International Publishing. 1
- [17] Jeffrey Mahler, Jacky Liang, Sherdil Niyaz, Michael Laskey, Richard Doan, Xinyu Liu, Juan Aparicio Ojea, and Ken Goldberg. Dex-net 2.0: Deep learning to plan robust grasps with synthetic point clouds and analytic grasp metrics. In *Robotics: Science and Systems (RSS)*, 2017. 2
- [18] Gilles Maximilian, Yuhao Chen, Tim Robin Winter, E. Zhixuan Zeng, and Alexander Wong. MetaGraspNet: A large-scale benchmark dataset for scene-aware ambidextrous bin picking via physics-based metaverse synthesis. In *IEEE International Conference on Automation Science and Engineering (CASE)*, 2022. 4
- [19] Peter Ochs, Jitendra Malik, and Thomas Brox. Segmentation of moving objects by long term video analysis. *IEEE Transactions on Pattern Analysis and Machine Intelligence*, 36(6): 1187–1200, 2014. 7, 1
- [20] F. Perazzi, J. Pont-Tuset, B. McWilliams, L. Van Gool, M. Gross, and A. Sorkine-Hornung. A benchmark dataset and evaluation methodology for video object segmentation. In *2016 IEEE Conference on Computer Vision and Pattern Recognition (CVPR)*, pages 724–732, 2016. 1
- [21] Lu Qi, Li Jiang, Shu Liu, Xiaoyong Shen, and Jiaya Jia. Amodal instance segmentation with kins dataset. In *2019 IEEE/CVF Conference on Computer Vision and Pattern Recognition (CVPR)*, pages 3009–3018, 2019. 7
- [22] Weichao Qiu and Alan Yuille. Unrealv: Connecting computer vision to unreal engine. In *Computer Vision – ECCV 2016 Workshops*, pages 909–916, Cham, 2016. Springer International Publishing. 3
- [23] Andreas Richtsfeld, Thomas Mörwald, Johann Prankl, Michael Zillich, and Markus Vincze. Segmentation of unknown objects in indoor environments. In *2012 IEEE/RSJ International Conference on Intelligent Robots and Systems*, pages 4791–4796, 2012. 3, 6
- [24] Markus Suchi, Timothy Patten, David Fischinger, and Markus Vincze. Easylabel: A semi-automatic pixel-wise object annotation tool for creating robotic rgb-d datasets. In *2019 International Conference on Robotics and Automation (ICRA)*, pages 6678–6684, 2019. 3, 6

- [25] Josh Tobin, Rachel Fong, Alex Ray, Jonas Schneider, Wojciech Zaremba, and Pieter Abbeel. Domain randomization for transferring deep neural networks from simulation to the real world. In *2017 IEEE/RSJ International Conference on Intelligent Robots and Systems (IROS)*, pages 23–30, 2017. [3](#)
- [26] Emanuel Todorov, Tom Erez, and Yuval Tassa. Mujoco: A physics engine for model-based control. In *2012 IEEE/RSJ International Conference on Intelligent Robots and Systems*, pages 5026–5033, 2012. [3](#)
- [27] Fanbo Xiang, Yuzhe Qin, Kaichun Mo, Yikuan Xia, Hao Zhu, Fangchen Liu, Minghua Liu, Hanxiao Jiang, Yifu Yuan, He Wang, Li Yi, Angel X. Chang, Leonidas J. Guibas, and Hao Su. Sapien: A simulated part-based interactive environment. In *2020 IEEE/CVF Conference on Computer Vision and Pattern Recognition (CVPR)*, pages 11094–11104, 2020. [3](#)
- [28] Christopher Xie, Yu Xiang, Arsalan Mousavian, and Dieter Fox. The best of both modes: Separately leveraging rgb and depth for unseen object instance segmentation. In *Proceedings of the Conference on Robot Learning*, pages 1369–1378. PMLR, 2020. [2](#), [3](#), [7](#), [1](#)
- [29] Xinchun Yan, Jasmined Hsu, Mohammad Khansari, Yunfei Bai, Arkanath Pathak, Abhinav Gupta, James Davidson, and Honglak Lee. Learning 6-dof grasping interaction via deep geometry-aware 3d representations. In *2018 IEEE International Conference on Robotics and Automation (ICRA)*, pages 3766–3773, 2018. [2](#)
- [30] Hanbo Zhang, Xuguang Lan, Site Bai, Xinwen Zhou, Zhiqiang Tian, and Nanning Zheng. Roi-based robotic grasp detection for object overlapping scenes. In *2019 IEEE/RSJ International Conference on Intelligent Robots and Systems (IROS)*, pages 4768–4775, 2019. [2](#)
- [31] Chuanxia Zheng, Duy-Son Dao, Guoxian Song, Tat-Jen Cham, and Jianfei Cai. Visiting the invisible: Layer-by-layer completed scene decomposition. *International Journal of Computer Vision*, 2021. [2](#)

SynTable: A Synthetic Data Generation Pipeline for Unseen Object Amodal Instance Segmentation of Cluttered Tabletop Scenes

Supplementary Material

7. Overview

This supplementary material offers dataset visualization, qualitative results, and additional technical details to support the main paper. Section 8 provides a comprehensive elaboration of the evaluation metrics employed. Section 9 illustrates how occlusion order accuracy is calculated and the validity of the metric. Furthermore, Section 10 delineates the process of generating an occlusion order directed acyclic graph from the occlusion order adjacency matrix to classify objects in three distinct order layers. Lastly, Section 11 showcases some qualitative inference results of UOAIS-Net on the OSD-Amodal dataset. Section 12 presents additional results from our experiments in Section 5 of the main paper. These experiments were conducted by training and evaluating AmodalMRCNN, ORCNN and, ASN on the same datasets as UOAIS-Net. The results observed from the experiments are consistent with our claims in the main paper and further demonstrate the capability of SynTable to improve the performance of a variety of different UOAIS models.

7.1. Video Demonstration of SynTable-Sim Generation Process

In addition to this document, we include a demonstration video as part of our supplementary material to demonstrate in detail the process of generating a custom synthetic dataset using SynTable. We refer readers to the demonstration video for a detailed visualization of the dataset generation process. The video can be found at <https://www.youtube.com/watch?v=zHM8H58Kn3E>.

7.2. Management of the SynTable-Sim Dataset

All the CAD models of the objects used in our SynTable-Sim dataset, as well as the dataset itself, are hosted in the Zenodo open repository, free for all to download. The DOI of our dataset is [10.5281/zenodo.10565517](https://doi.org/10.5281/zenodo.10565517). The dataset can be accessed at <https://doi.org/10.5281/zenodo.10565517>

8. Details about Evaluation Metrics

In this paper, we employ the precision/recall/F-measure (P/R/F) metrics, as defined in [6, 19, 28]. This metric favors methods that accurately segment the desired objects while penalizing those that produce false positives. Specifically, the precision, recall, and F-measure are calculated between all pairs of predicted and ground truth objects. The Hun-

garian method, employing pairwise F-measure, is utilized to establish a match between predicted objects and ground truth. Given this matching, the Overlap P/R/F is computed by:

$$P = \frac{\sum_i |c_i \cap g(c_i)|}{\sum_i |c_i|}, \quad R = \frac{\sum_i |c_i \cap g(c_i)|}{\sum_j |g_j|} \quad (9)$$

$$F = \frac{2PR}{P+R} \quad (10)$$

where c_i denotes the set of pixels belonging to predicted object i , $g(c_i)$ is the set of pixels of the matched ground truth object of c_i after Hungarian matching, and g_j is the set of pixels for ground truth object j .

Although the aforementioned metric provides valuable information, it fails to consider the boundaries of the objects. Therefore, Xie *et al.* [28] proposed the Boundary P/R/F measure to supplement the Overlap P/R/F. The calculation of Boundary P/R/F involves the same Hungarian matching as used in the computation of Overlap P/R/F. Given these matchings, the Boundary P/R/F is computed by:

$$P = \frac{\sum_i |c_i \cap D[g(c_i)]|}{\sum_i |c_i|}, \quad R = \frac{\sum_i |D[c_i] \cap g(c_i)|}{\sum_j |g_j|} \quad (11)$$

$$F = \frac{2PR}{P+R} \quad (12)$$

Here, overloaded notations are used to represent the sets of pixels belonging to the boundaries of the predicted object i and the ground truth object j as c_i and g_j , respectively. The dilation operation is denoted by $D[\cdot]$, which allows for some tolerance in the prediction. The metrics we use are a combination of the F-measure described in [20] and the Overlap P/R/F as defined in [6].

In our work, we use the Overlap and Boundary P/R/F evaluation metrics to evaluate the accuracy of the predicted visible, invisible, and amodal masks. In the context of the Overlap P/R/F metrics, c_i denotes the set of pixels belonging to the predicted visible, invisible, and amodal masks, $g(c_i)$ denotes the set of pixels belonging to the matched ground-truth visible, invisible and amodal masks annotations, and g_j is the ground-truth visible, invisible and amodal mask. The meaning of c_i , $g(c_i)$, and g_j are similar in the context of the Boundary P/R/F metrics.

An additional vital evaluation metric used in our paper is the $F@.75$. This metric represents the proportion of segmented objects with an Overlap F-measure greater than

0.75. It is important not to confuse this metric with the F-measure computed for the Overlap and Boundary P/R/F. The F-measure for Overlap and Boundary is a harmonic mean of a model’s average precision and average recall, while $F@.75$ indicates the percentage of objects from a dataset that can be segmented with high accuracy. The F in $F@.75$ refers to the F-measure computed for a ground truth object after the Hungarian matching of the ground truth mask j with the predicted mask i as defined in [6] and stated in Equation (14).

$$P_{ij} = \frac{|c_i \cap g_j|}{|c_i|}, \quad R_{ij} = \frac{|c_i \cap g_j|}{|g_j|} \quad (13)$$

$$F_{ij} = \frac{2P_{ij}R_{ij}}{P_{ij} + R_{ij}} \quad (14)$$

The notation c_i denotes the set of pixels that belong to a predicted region i , while g_j represents all the pixels that belong to a non-background ground truth region j . In addition, P_{ij} represents the precision score, R_{ij} represents the recall score, and F_{ij} represents the F-measure score that corresponds to this particular pair of predicted and ground truth regions.

9. Occlusion Order Accuracy ACC_{oo} metric

Given an image v that depicts a typical cluttered tabletop scene, we get the ground truth-prediction assignment pairs after Hungarian matching as illustrated in Figure 7. The predicted masks will then be re-indexed to match the ids of the ground truth masks. Following that, the *predVisible* and *predOcclusion* masks that belong to the assigned pairs will be extracted. After that, the ground truth OOAM (*gtOOAM*) and the predicted OOAM (*predOOAM*) will be obtained using Algorithm 1.

Figure 7 also illustrates the calculation of occlusion order accuracy in an image v . The similarity matrix (denoted as *similarityMatrix* in Figure 7) is obtained by conducting an element-wise equality comparison between the *gtOOAM* and *predOOAM*. After that, ACC_{oo} can be calculated using Equation 8.

In Equation 8, the ACC_{oo} represents the ratio of the number of correct predicted occlusion nodes over the number of ground truth occlusion nodes. Let *#correctPredictedOcclusionNodes* denote the number of correct occluder and occludee predictions for all objects in a viewpoint (represented by green highlighted cells in *similarityMatrix* in Figure 7).

A summation of all the elements in the similarity matrix is carried out to obtain *#correctPredictedOcclusionNodes*. Let *#groundtruthOcclusionNodes* denote the number of ground truth occluder and occlude nodes in a viewpoint. To obtain *#groundtruthOcclusionNodes*, we count the number of elements (*gtOOAMSize*) in the ground truth OOAM. As an object cannot occlude itself, the diagonal of

any OOAM is always 0, and the diagonal of any similarity matrix is always 1 (depicted as grey highlighted cells in Figure 7). Thus, we subtract the number of elements along the diagonal of the *gtOOAM* (denoted by *gtOOAMDiagonalSize*) from the calculation of *#correctPredictedOcclusionNodes* and *#groundtruthOcclusionNodes*.

Correct occlusion order predictions occur when the predicted occlusion relationship for each object matches the ground truth. Incorrect occlusion order predictions can result from erroneous predictions or missing visible mask predictions of object instances. When there are missing predictions, setting the corresponding row and column of the missing object instance in the similarity matrix to 0 penalizes the model for the missing object predictions. The smaller element-wise sum of the similarity matrix leads to a smaller ACC_{oo} . This demonstrates the appropriate assignment of penalties by ACC_{oo} to different error types for measuring object occlusion ordering in a scene, highlighting its significance in the context of scene understanding for robotic grasp planning.

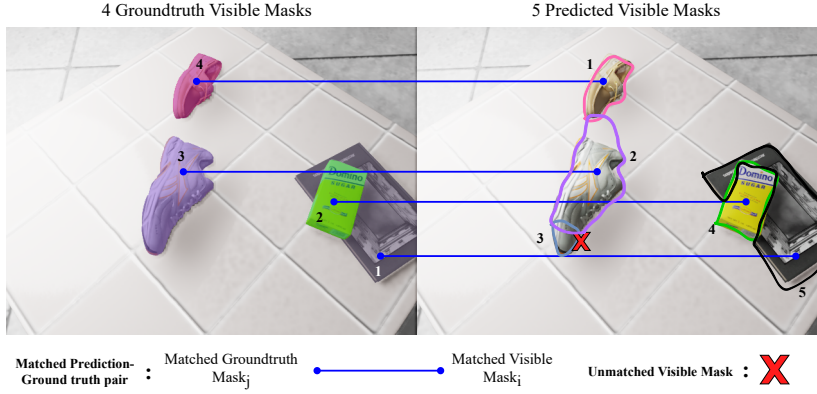
10. Occlusion Order Directed Acyclic Graph (OODAG)

After obtaining the Occlusion Order Adjacency Matrix (OOAM), we can generate the occlusion order directed graph from it. For each non-zero entry (i, j) in the OOAM, we draw a directed edge from node i to node j . If the entry is zero, we do not draw an edge. A non-zero entry at (i, j) represents that object i is occluding object j .

For example, the OOAM generated in Figure 8 shows that $(i, j) = (1, 12)$ where i and j are the object indices (the bounding box labels) in the image. This means that object 1 occludes object 12, and a directed edge will point from object 1 to 12. From the generated Directed Occlusion Graph, we can also check if the graph is cyclic or acyclic using graph cyclic detection methods such as Depth First Search (DFS) and Breadth First Search (BFS). Only if the graph has no directed cycles (Directed Acyclic Occlusion Graph) can topological sorting be implemented to find the picking sequence to grasp all objects in the scene safely.

In the generated Occlusion Order graph, we further classify objects in three different order layers - Top, Intermediate, and Bottom. Objects at the top layer represent objects that are not occluded by any other object and can be grasped directly. Objects in the intermediate layers mean that they are occluded but they also occlude other objects. For objects in the bottom layer, they are occluded but they do not occlude other objects.

Get best assignment of prediction masks to groundtruth mask that maximises the F-measure



F-Measure table

		predicted mask i				
		1	2	3	4	5
ground truth mask j	1	0	0	0	0.12	0.87
	2	0	0	0	0.95	0.08
	3	0	0.74	0.28	0	0
	4	0.94	0.06	0	0	0

Blue highlighted cells represent highest F-measure for a ground truth - predicted mask pair

After Hungarian matching, matched pairs are as follows:
 ground truth object ids (1, 2, 3, 4)
 predicted object ids (5, 4, 2, 1).
 predicted object ids are re-indexed to (1,2,3,4).



Element Wise Comparison

$$\begin{matrix}
 \left. \begin{matrix}
 \text{occludee} \\
 \begin{matrix}
 1 & 2 & 3 & 4 \\
 0 & 1 & 0 & 0 \\
 1 & 0 & 0 & 0 \\
 0 & 0 & 0 & 1 \\
 0 & 0 & 0 & 0
 \end{matrix} \\
 \text{occluder} \\
 \text{predOOAM}_v
 \end{matrix} \right\}
 \begin{matrix}
 = \\
 \begin{matrix}
 \text{occludee} \\
 \begin{matrix}
 1 & 2 & 3 & 4 \\
 0 & 0 & 0 & 0 \\
 1 & 0 & 0 & 0 \\
 0 & 0 & 0 & 0 \\
 0 & 0 & 0 & 0
 \end{matrix} \\
 \text{occluder} \\
 \text{gtOOAM}_v
 \end{matrix}
 \end{matrix}
 \right\}
 = \\
 \begin{matrix}
 \begin{matrix}
 1 & 0 & 1 & 1 \\
 1 & 1 & 1 & 1 \\
 1 & 1 & 1 & 0 \\
 1 & 1 & 1 & 1
 \end{matrix} \\
 \text{similarityMatrix}_v \\
 \text{sum}(\text{similarityMatrix}_v) = 14
 \end{matrix}
 \end{matrix}$$

$gtOOAMSize_v = 4 \times 4 = 16$
 $gtOOAMDiagonalSize_v = 4$
 $sum(similarityMatrix_v) = 14$

$$(ACC_{OO})_v = \frac{sum(similarityMatrix_v) - gtOOAMDiagonalSize_v}{gtOOAMSize_v - gtOOAMDiagonalSize_v} = \frac{14 - 4}{16 - 4} = 0.83$$

Figure 7. Hungarian Matching and calculating Occlusion Order Accuracy of image v

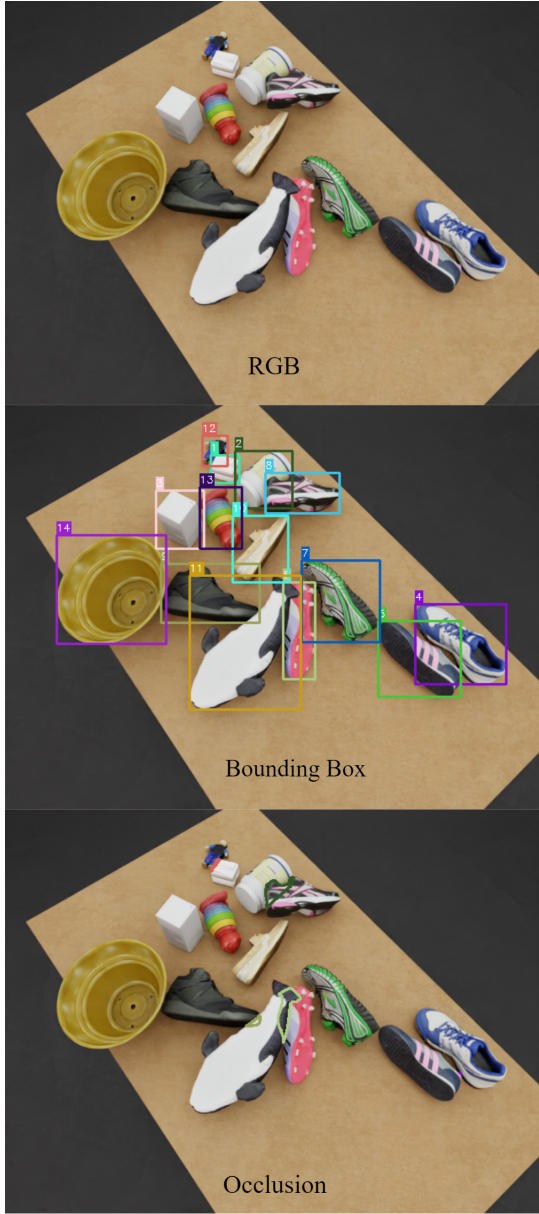
11. Qualitative Inference Results of UOAI-Net on the OSD-Amodal Dataset

After training the UOAI-Net model [2] on both SynTable-Sim and UOAI-Sim (tabletop) datasets [2], we present some of our qualitative results in Figure 9. As discussed in the main text of our paper, the UOAI-Net trained on the SynTable-Sim dataset exhibits superior performance in contrast to the UOAI-Net trained on the UOAI-Sim tabletop dataset. This observation is further supported by the inference results presented in Figure 9. Furthermore, as the scene becomes more and more cluttered, the UOAI-Net model trained on the SynTable-Sim dataset evidently out-

performs that of the UOAI-Net trained on the UOAI-Sim tabletop dataset. In the context of robotic grasping on cluttered tabletops, foreground masking algorithms can be utilized to filter out the background and out-of-the-table predicted object instances.

12. Additional Quantitative Inference Results on the OSD-Amodal Dataset

We also evaluated the effectiveness of SynTable-Sim across different UOAI models comprising distinct architectures. Table 5 compares the performance of UOAI models—Amodal MRCNN, ORCNN, ASN, and UOAI-Net—on



	Occludee													
	1	2	3	4	5	6	7	8	9	10	11	12	13	14
1	0	0	0	0	0	0	0	0	0	0	0	1	0	0
2	0	0	0	0	0	0	0	0	0	0	0	0	0	0
3	0	0	0	0	0	0	0	0	0	0	0	0	0	0
4	0	0	0	0	0	0	0	0	0	0	0	0	0	0
5	0	0	0	1	0	0	0	0	0	0	0	0	0	0
6	0	0	0	0	0	0	0	0	0	0	0	0	0	0
7	0	0	0	0	0	0	0	0	0	0	0	0	0	0
8	1	0	0	0	0	0	0	0	0	0	0	0	0	0
9	0	0	0	0	0	0	0	0	0	0	0	0	0	0
10	0	0	0	0	0	0	0	0	0	0	0	0	0	0
11	0	0	0	0	1	0	0	1	0	0	0	0	0	0
12	0	0	0	0	0	0	0	0	0	0	0	0	0	0
13	0	0	0	0	0	0	0	0	0	0	0	0	0	0
14	0	0	0	0	0	0	0	0	0	0	0	0	0	0

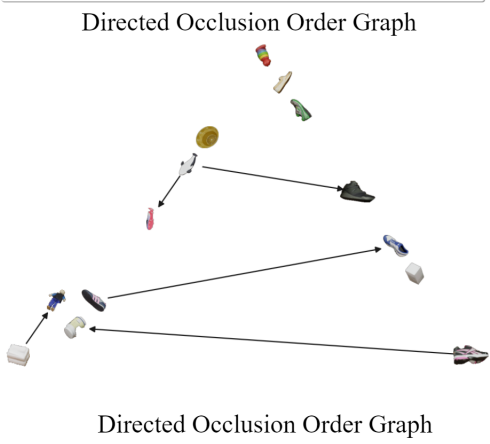
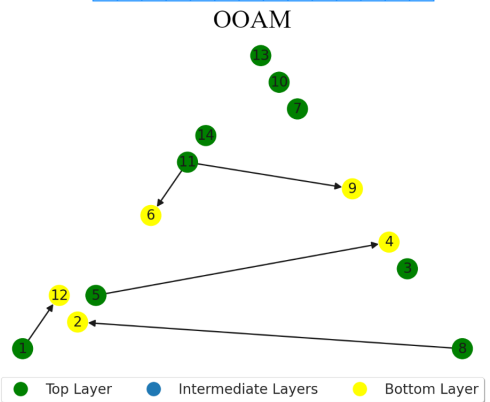


Figure 8. A visualisation of annotations for a cluttered tabletop image generated by SynTable

the OSD-Amodal dataset after training on the UOAI-Sim tabletop dataset and our SynTable-Sim sample dataset. For each model result in our experiments, we used seed 7 for training. Generally, across most metrics, the UOAI models trained on SynTable-Sim outperform the same models trained on the UOAI-Sim tabletop dataset. There is also a significant improvement in the results of ACC_{oo} for Amodal MRCNN, ORCNN, and ASN when trained on our SynTable-Sim as compared to the UOAI-Sim tabletop dataset. This is consistent with the performance trend observed for UOAI-Net and, therefore, demonstrates that

SynTable is an effective tool for generating high-quality datasets that can improve the performance of UOAI models. A detailed breakdown of the precision P, recall R, and F-measure F, and $F@.75$ scores for the amodal, invisible, and visible masks are shown in Table 6.

As shown in Table 7, the UOAI models trained on the SynTable-Sim dataset outperform the same models trained on the UOAI-Sim tabletop dataset in all metrics when they are benchmarked on the SynTable-Sim validation dataset.

Table 5. The performance of Amodal MRCNN, ORCNN, ASN, and UOAIIS-Net on the **OSD-Amodal dataset** after training on the UOAIIS-Sim and SynTable-Sim datasets. UOAIIS-Net is trained with RGB-D images. **OV**: Overlap F-measure, **BO**: Boundary F-measure, **F@.75**: Percentage of segmented objects with an Overlap F-measure greater than 0.75, **ACC_{OO}**: Occlusion Order Accuracy

Training Set	Method	Amodal Mask			Invisible Mask			Occlusion		Visible Mask			ACC _{OO}
		OV	BO	F@.75	OV	BO	F@.75	F _ℓ	ACC _ℓ	OV	BO	F@.75	
UOAIIS-Sim (Tabletop)	Amodal MRCNN	36.7	26.9	45.7	8.8	4.8	7.7	39.2	54.8	38.7	26.3	32.2	15.6
	ORCNN	36.3	25.4	47.0	12.2	6.7	9.0	43.8	59.2	30.5	21.8	29.6	21.5
	ASN	40.5	33.6	49.8	17.4	12.1	15.0	47.0	63.2	39.3	31.6	36.8	17.8
	UOAIIS-Net	49.0	50.3	82.7	42.3	23.9	40.3	68.9	84.0	47.3	50.0	70.6	80.4
SynTable-Sim (Ours)	Amodal MRCNN	74.5	57.5	77.2	41.3	23.5	37.6	69.3	79.4	73.8	57.7	66.1	79.2
	ORCNN	74.2	58.2	77.1	44.7	24.3	33.8	72.9	82.2	72.0	58.3	67.7	79.1
	ASN	78.2	60.2	75.3	46.4	27.7	35.8	72.6	83.0	78.1	61.8	68.9	80.2
	UOAIIS-Net	64.4	51.5	84.3	47.3	24.2	47.4	60.0	91.9	65.3	53.7	78.2	87.0

Table 6. A breakdown of the precision, recall, and F-measure of the amodal, invisible, and visible mask predictions by Amodal MRCNN, ORCNN, ASN, and UOAIIS-Net on the **OSD-Amodal dataset** after training on the UOAIIS-Sim and SynTable-Sim dataset. **P**: Precision, **R**: Recall, **F**: F-measure

Training Set	Method	Amodal Mask							Invisible Mask							Visible Mask						
		Overlap			Boundary			F@.75	Overlap			Boundary			F@.75	Overlap			Boundary			F@.75
		P	R	F	P	R	F		P	R	F	P	R	F		P	R	F	P	R	F	
UOAIIS-Sim (Tabletop)	Amodal MRCNN	27.9	66.7	36.7	22.5	39.8	26.9	45.7	20.2	24.9	8.8	16.4	19.9	4.8	7.7	30.1	60.5	38.7	22.0	37.8	26.3	32.2
	ORCNN	26.3	71.1	36.3	19.8	42.4	25.4	47.0	41.5	22.7	12.2	33.9	17.9	6.7	9.0	21.4	63.4	30.5	16.6	38.2	21.8	29.6
	ASN	31.7	67.8	40.5	28.6	45.4	33.6	49.8	47.6	23.4	17.4	38.8	20.2	12.1	15.0	32.0	63.5	39.3	28.2	41.5	31.6	36.8
	UOAIIS-Net	37.2	85.5	49.0	41.1	71.3	50.3	82.7	50.9	54.0	42.3	24.8	41.1	23.9	40.3	35.4	81.6	47.3	41.3	69.3	50.0	70.6
SynTable-Sim (Ours)	Amodal MRCNN	72.3	81.6	74.5	54.6	64.5	57.5	77.2	54.9	48.0	41.3	30.3	38.8	23.5	37.6	72.1	78.4	73.8	55.1	63.7	57.7	66.1
	ORCNN	73.7	80.8	74.2	55.6	64.5	58.2	77.1	61.0	47.1	44.7	31.1	38.6	24.3	33.8	69.8	79.1	72.0	55.7	64.3	58.3	67.7
	ASN	78.2	80.3	78.2	57.8	64.9	60.2	75.3	65.2	46.2	46.4	32.9	38.7	27.7	35.8	77.5	80.1	78.1	60.4	65.4	61.8	68.9
	UOAIIS-Net	53.9	86.3	64.4	40.9	74.6	51.5	84.3	53.0	60.0	47.3	20.5	48.3	24.2	47.4	55.0	86.2	65.3	43.2	75.3	53.7	78.2

Table 7. The performance of Amodal MRCNN, ORCNN, ASN, and UOAIIS-Net on the **SynTable-Sim validation dataset** after training on the UOAIIS-Sim and SynTable-Sim datasets. UOAIIS-Net is trained with RGB-D images. **OV**: Overlap F-measure, **BO**: Boundary F-measure, **F@.75**: Percentage of segmented objects with an Overlap F-measure greater than 0.75, **ACC_{OO}**: Occlusion Order Accuracy

Training Set	Method	Amodal Mask			Invisible Mask			Occlusion		Visible Mask			ACC _{OO}
		OV	BO	F@.75	OV	BO	F@.75	F _ℓ	ACC _ℓ	OV	BO	F@.75	
UOAIIS-Sim (Tabletop)	Amodal MRCNN	27.1	25.2	23.8	6.7	6.2	3.5	35.8	66.0	29.1	26.2	23.5	19.0
	ORCNN	30.9	29.0	28.1	12.5	11.4	8.0	39.9	68.4	31.8	30.2	27.3	23.1
	ASN	33.3	34.4	35.3	10.3	9.1	5.0	47.6	72.3	35.0	36.0	34.1	31.6
	UOAIIS-Net	39.9	40.5	38.6	17.0	15.5	9.6	49.6	74.9	41.6	40.7	35.9	31.6
SynTable-Sim (Ours)	Amodal MRCNN	83.5	76.2	72.5	35.4	31.8	16.4	73.2	80.3	85.7	79.1	71.1	72.8
	ORCNN	83.4	76.0	72.2	34.4	29.3	15.3	67.2	73.7	85.3	78.9	70.9	73.0
	ASN	83.6	76.9	73.9	38.5	35.1	18.5	74.8	81.5	86.1	80.0	72.8	75.8
	UOAIIS-Net	83.7	77.5	75.1	40.3	36.7	20.2	75.5	82.0	86.2	80.1	73.3	77.4

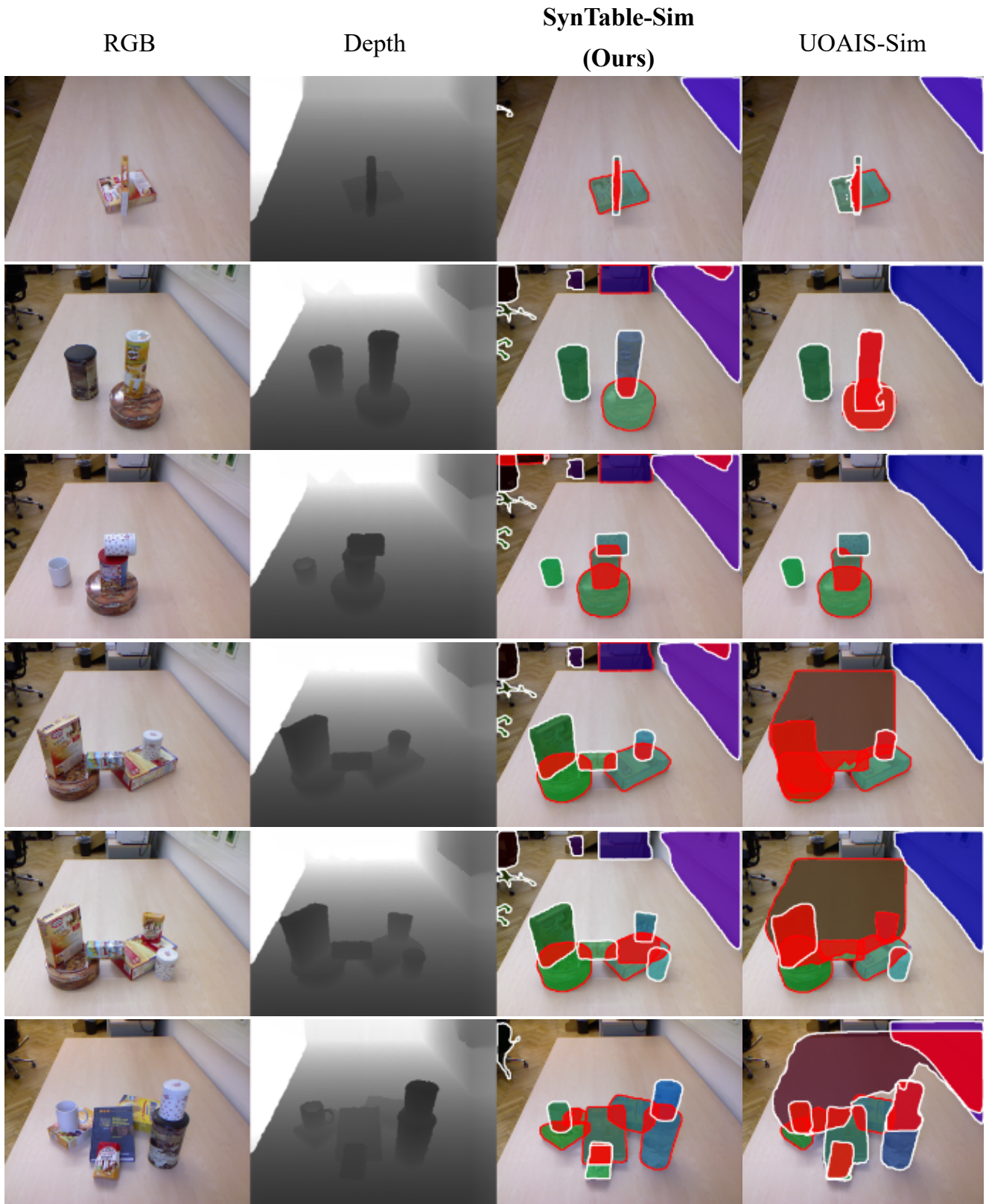


Figure 9. Comparison of the inference results on the OSD-Amodal dataset. **SynTable-Sim (Ours)**: the performance of UOAI-Sim on the OSD-Amodal dataset after training on the SynTable-Sim dataset. **UOAI-Sim**: the performance of UOAI-Sim on the OSD-Amodal dataset after training on the UOAI-Sim tabletop dataset.